

The Cluster Galaxy Circular Velocity Function

V. Desai ^{*}, J. J. Dalcanton [†], L. Mayer, D. Reed, T. Quinn, F. Governato [‡]

University of Washington Department of Astronomy, Box 351580, Seattle WA 98195-1580, USA

ABSTRACT

We present galaxy circular velocity functions (GCVFs) for 34 low redshift ($z \lesssim 0.15$) clusters identified in the Sloan Digital Sky Survey (SDSS), for fifteen clusters drawn from dark matter simulations of hierarchical structure growth in a Λ CDM cosmology, and for $\sim 29,000$ SDSS field galaxies. We find that the observed and simulated cluster GCVFs take the form of a power law. The cumulative GCVFs of the simulated clusters are very similar across a wide range of cluster masses, provided individual subhalo circular velocities are scaled by the circular velocities of the parent cluster. Once all sources of error are accounted for, the intrinsic scatter in the cumulative, scaled observed cluster GCVF is consistent with the simulations. The slope of the observed cluster GCVF is ~ -2.5 , independent of cluster velocity dispersion. The average slope of the simulated GCVFs is somewhat steeper, although formally consistent given the errors. Using our highest resolution cluster, we find that the effects of baryons on galaxy rotation curves is to flatten the simulated cluster GCVF into better agreement with observations. Finally, we find that the field GCVF deviates significantly from a power law, being flatter than the cluster GCVF at circular velocities less than 200 km s^{-1} , and steeper at circular velocities greater than 200 km s^{-1} .

Key words: cosmology: theory — cosmology: observations — galaxies: halos — galaxies: clusters — methods: N -body simulations — dark matter.

1 INTRODUCTION

In the widely accepted hierarchical clustering model of structure formation, adiabatic fluctuations in the initial density field grow and merge into increasingly larger dark matter halos. Simple inflationary approaches model the initial power spectrum of fluctuations as Gaussian and scale-invariant, while cosmological parameters and the nature of the dark matter control its subsequent evolution. The resulting mass function of dark matter halos can be predicted using N -body simulations (Sheth & Tormen 1999; Bode et al. 2001; Jenkins et al. 2001; Reed et al. 2003) or analytic methods based upon Press-Schechter theory (Press & Schechter 1974; Bond et al. 1991; Bower 1991; Lacey & Cole 1993; Sheth, Mo & Tormen 2001). The observed mass function is therefore an important constraint on fundamental properties of the universe. In the following, we focus on the mass function on galaxy scales.

Comparing predicted mass functions to observations requires mapping the observable properties of galaxies onto the masses of their dark matter halos. In one technique, semi-analytic models (SAMs) are used to predict the luminosities of galaxies within halos of different masses, by

parametrizing models of the complicated processes of gas cooling, star formation, stellar evolution, and feedback. These techniques efficiently explore a wide variety of models. However, their utility is limited by the extent to which the simple recipes capture the relevant physics.

An alternative to SAMs utilizes the empirical relationship between velocities and luminosities in both spiral and elliptical galaxies to transform the observed galaxy luminosity function into a galaxy circular velocity function (GCVF), which is closely related to the mass function (Cole & Kaiser 1989; Shimasaku 1993; Gonzalez et al. 2000; Kochanek & White 2001). While this approach avoids a number of assumptions required to assign luminosities to dark matter halos, baryons cannot be completely ignored. The baryonic mass distribution affects a galaxy's circular velocity profile significantly, while also changing the equilibrium configuration of the host dark matter halo through adiabatic contraction (Blumenthal et al. 1986). Baryons also determine the probability that a galaxy will be included in a given observational sample. However, the circular velocity directly traces the total enclosed mass of a galaxy, which is dominated by dark matter at sufficiently large radii. Therefore, models of the GCVF are less sensitive to inaccuracies in our understanding of star formation, stellar evolution, and feedback than those of the luminosity function. The observed GCVF therefore better constrains the mass function.

^{*} E-mail: desai@astro.washington.edu

[†] Alfred P. Sloan Research Fellow

[‡] David E. Brooks Research Fellow

Recent comparisons between observed and theoretical field GCVFs indicate that low-mass halos with circular velocities $\lesssim 200 \text{ km s}^{-1}$ are over-predicted by simulations (Gonzalez et al. 2000; Kochanek & White 2001). It is now possible to extend the analysis of the GCVF to galaxies within clusters. The current generation of N -body simulations (Ghigna et al. 1998; Tormen, Diaferio & Syer 1998; Klypin et al. 1999; Okamoto & Habe 2000; Springel et al. 2001) has achieved the force and mass resolution necessary to capture the effects of tidal stripping, dynamical friction, and galaxy harassment, essential for predicting the GCVF in dense environments. Moore et al. (1999) used the Tully-Fisher relation to determine circular velocities for galaxies in the Virgo Cluster. They compared the resulting distribution to that in a standard CDM simulation of a Virgo-like cluster, and found good agreement down to $\sim 50 \text{ km s}^{-1}$ without accounting for the effects of baryons on galaxy rotation curves. Coupling dark matter merging trees with SAMs which include strong feedback, Springel et al. (2001) were able to reproduce a wide variety of cluster properties. Although they did not directly compute the cluster GCVF, the agreement between a variety of observed and modeled cluster relations (morphology-density, luminosity function, Tully-Fisher, Faber Jackson) suggests that they would have found agreement for the cluster GCVF as well. Although these works represent significant progress in testing simulations of cluster substructure against observations, larger samples of both simulations and observations are required to assess whether the results are typical, and over what cluster mass range.

Toward this goal, we determine the GCVFs for 34 nearby clusters from the Sloan Digital Sky Survey (SDSS). To compare the observed clusters to theoretical predictions, we assemble a sample of 15 high resolution cluster simulations, from which we measure the theoretical cluster GCVF. We also repeated the GCVF analysis for $\sim 29,000$ galaxies from the SDSS, to allow a comparison to the field.

Our method for determining the GCVFs for the SDSS sample is described in §2. In §3 we describe the simulations. Our results are discussed in §4. First we discuss the shape of the cluster GCVF as related to that of the cluster luminosity function (§4.1). Second, we investigate the claim of Moore et al. (1999) that the velocity distribution of substructure on all mass scales is self-similar when scaled by the host halo velocity (§4.2). Third, we present power-law fits to the cluster GCVF, quantify its dependence on cluster velocity dispersion, and make a comparison to dark matter cluster simulations (§4.3). Fourth, we examine how the adiabatic contraction of dark matter halos due to baryons affects the comparison between observed and simulated GCVFs (§4.4). Finally, we compare the observed cluster GCVF to that measured for the field (§4.5). A summary of our results can be found in §5.

Throughout we adopt $H_0 = 70 \text{ km s}^{-1} \text{ Mpc}^{-1}$, $\Lambda = 0.7$, and $\Omega = 0.3$.

2 METHODS: CONSTRUCTION OF THE OBSERVED CLUSTER GALAXY CIRCULAR VELOCITY FUNCTION

To construct the observed cluster GCVF, we use existing cluster catalogs and data from the SDSS. For each cluster, we calculate the characteristic circular velocities for galaxies within the virial radius, using the Tully-Fisher and Fundamental Plane relations. Note that this is done galaxy-by-galaxy, rather than by transforming the luminosity function, as has been done previously (Cole & Kaiser 1989; Gonzalez et al. 2000; Kochanek & White 2001). In this section, we describe the SDSS, the cluster catalogs, our determination of global cluster properties, the application of the Tully-Fisher and Fundamental Plane relations, the completeness velocities of the resulting GCVFs, and our background subtraction procedure.

2.1 The Sloan Digital Sky Survey

The Sloan Digital Sky Survey (SDSS; York et al. 2000) is a photometric and spectroscopic survey being carried out at the Apache Point Observatory using a 2.5-m telescope equipped with modern CCD detectors (Gunn et al. 1998). This ambitious project will eventually cover the Northern Galactic Hemisphere, almost one quarter of the sky. The photometric survey provides nearly simultaneous imaging in five passbands (u, g, r, i, z ; Fukugita et al. 1996). The spectroscopic survey consists of medium resolution ($\lambda/\Delta\lambda = 2000$) spectra of galaxies, quasars, and stars selected systematically from the photometric catalogs.

The first public release of SDSS data occurred in June 2001, and is known as the Early Data Release (EDR; Stoughton et al. 2002). The EDR consists of imaging data covering approximately 460 square degrees of sky, as well as approximately 55,000 spectra.

The photometric and spectroscopic pipelines (Lupton et al. 2001; Stoughton et al. 2002) measure numerous quantities that are available as part of the EDR. Below we describe only those which will be used in the present analysis. Note that because the photometric system has yet to be finalized, we denote the current, temporary magnitudes with asterisks, while references to the bandpasses remain simply italicized.

The photometric pipeline computes two types of magnitudes appropriate for use on galaxies: Petrosian and model. Petrosian magnitudes attempt to measure a constant fraction of the total light of a galaxy, independent of surface brightness, distance, or photometric model. The Petrosian radius is computed in the r band, and Petrosian magnitudes in all bands are based upon the amount of flux within two Petrosian radii. High signal-to-noise measurements of the Petrosian magnitude can be made for galaxies as faint as $r^* \sim 20$. As Petrosian magnitudes become noisy, model magnitudes provide a more robust estimate of the total light of a galaxy. To compute model magnitudes, the photometric pipeline fits a pure de Vaucouleurs profile and a pure exponential profile to the two dimensional r image of each galaxy. The best-fitting model is then applied, up to an amplitude change, to images in the other bands. All fits account for the effects of local seeing. Parameters derived from these fits include `r.deV`, half the length of the major axis of the

ellipse that encloses half the light of the galaxy; and `ab_exp` and `ab_deV`, the best-fitting minor-to-major axis ratios for the two models.

A bug in the SDSS photometric pipeline causes the model magnitudes of bright galaxies to be ~ 0.2 magnitudes too bright. The inverse Fundamental Plane relation we use to estimate the circular velocities of early type galaxies (§2.4.2) was calibrated using model magnitudes afflicted by the same bug. We therefore continue in the use of EDR model magnitudes for early types in order to remain consistent with this calibration. The inverse Tully-Fisher relation we apply to late type galaxies (2.4.1) was calibrated using magnitudes extrapolated to infinity assuming exponential surface brightness profiles. Correctly-calculated model magnitudes would be the optimal choice for consistency with this calibration. In their absence, we use Petrosian magnitudes for late type galaxies.

We adopt galactic extinction corrections as functions of position based upon Schlegel, Finkbeiner & Davis (1998), and available from the SDSS database as the `reddening` parameter. All magnitudes in the remainder of this paper refer to reddening-corrected values.

The spectroscopic pipeline determines both an emission and cross-correlation redshift. Final redshifts (z) are assigned to each galaxy by choosing the method with the highest confidence interval.

2.2 Cluster Sample

Several cluster catalogs have been constructed from SDSS data, using a variety of identification algorithms (Bahcall et al. 2003). In order to compute accurate GCVFs down to the lowest possible circular velocities, we used the nearest clusters. Miller et al., 2002 (in prep) have identified 62 clusters in the Equatorial Stripes of the SDSS using the C4 algorithm (Nichol et al. 2001; Gomez et al. 2002). This algorithm uses the observed phenomenon that galaxies in clusters have similar colors as well as locations. For each galaxy, the algorithm determines the number of neighbors in the seven-dimensional space spanning RA, DEC, redshift, and the four SDSS colors. This number of neighbors is compared to the distribution found for 100 random field galaxies. Based upon this comparison, the probability that the galaxy is a field galaxy is computed. Galaxies that are probably not field galaxies are identified using the False Discovery Rate thresholding technique (Miller et al. 2001).

In order to create as large a sample as possible, we supplement the C4 clusters with 51 nearby NED¹ clusters in the same area.

After removing 18 duplicates between the C4 and NED catalogs, 5 clusters with virial radii which extend beyond the SDSS data limits (§2.3), 36 clusters (mostly NED) with fewer than 20 spectroscopically confirmed members (§2.3), and 20 clusters with data defects or that were not rich enough to yield high signal-to-noise GCVFs, we are left with 34 clusters, which are listed in Table 1.

2.3 Determination of Global Cluster Properties

As discussed in §1, the GCVF may depend on environment, and thus on cluster mass. While a reliable cluster mass estimate is difficult to obtain, the line-of-sight velocity dispersion, σ_{cl} , is relatively straightforward to measure, and can be used as a proxy for the mass. We calculate σ_{cl} using the following procedure.

All galaxies with spectroscopic redshifts within a radius of either 1.5 Mpc or the largest radius allowed by the extent of the data, whichever was smaller, were selected. Galaxies were ordered by recessional velocity, and gaps larger than 800 km s^{-1} were used to remove interlopers. A robust weighted gap estimator (Beers, Flynn & Gebhardt 1990) was used to determine σ_{cl} from the remaining velocities. This process was performed iteratively until the velocity dispersion stabilized. The resulting velocity dispersion was divided by a factor of $(1+z)$ to correct it to the cluster frame (Danese, de Zotti & di Tullio 1980). In order to ensure accurate estimates of σ_{cl} , we rejected 36 clusters with fewer than 20 confirmed members. Errors were estimated using bootstrap re-sampling, and are typically 10–20 per cent. The velocity dispersions and errors for each cluster can be found in Table 1, columns 4 and 5, and the bottom panel of Figure 2 shows the distribution of σ_{cl} .

In order to compare our circular velocity functions to each other and to models, we calculated them within a consistent aperture. The virial radius, R_{vir} , is a natural aperture to select. Girardi & Mezzetti (2001) present the following empirical relation between R_{vir} and σ_{cl} :

$$R_{\text{vir}} \sim \frac{0.0017\sigma}{(1+z)^{3/2}} \text{ (km}^{-1} \text{ s } h_{100}^{-1} \text{ Mpc)}. \quad (1)$$

Here R_{vir} is the radius within which the average density is equal to $\Delta \sim 200$ times the critical density. Virial radii computed from Equation 1 are listed in column 6 of Table 1. We did not recalculate σ_{cl} using galaxies only within the virial radius for two reasons. First, for many of the clusters, nearly all spectroscopically confirmed cluster members were contained within R_{vir} . Second, for the remainder of clusters, we wished to determine σ_{cl} using as many redshifts as possible.

2.4 Determination of Galaxy Circular Velocities

Each galaxy within R_{vir} and with $r^* < 21.5$ (the star/galaxy separation limit; Lupton et al. 2001) is given the designation of Early (E, S0, Sa) or Late (Sb, Sc, Irr) type. Strateva et al. (2001) find that $u^* - r^* < 2.22$ is optimal for separating these classes. For selecting early types, the completeness is 68 per cent, while the reliability is 81 per cent. For selecting late types, the completeness is 77 per cent, and the reliability is 96 per cent. We then translated the surface photometry of each galaxy into a circular velocity using the conversions described in the following two subsections.

2.4.1 Late Type Galaxies

Disk galaxies exhibit a tight correlation between luminosity and circular velocity. The Tully-Fisher relation (TFR) allows one to compute the former given the latter. We require the

¹ The NASA/IPAC Extragalactic Database (NED) is operated by the Jet Propulsion Laboratory, California Institute of Technology, under contract with the National Aeronautics and Space Administration.

Table 1. Galaxy Cluster Sample

RA h:m:s	DEC °:':"	z	σ_{cl} km s ⁻¹	$\Delta\sigma_{\text{cl}}$ km s ⁻¹	R_{vir} Mpc	V_{compl} km s ⁻¹	$\log_{10} N_{200}$	$\Delta \log_{10} N_{200}$	β	$\Delta\beta$	N'_{200}	$\Delta N'_{200}$
00:21:40.841	-0:55:34.17	0.105	370	71	0.77	65	-0.50	0.08	-1.47	0.35	-0.83 s	0.04
00:23:31.152	-0:48:10.08	0.063	540	97	1.20	50	-0.96	0.13	-3.20	0.50	-0.88	0.05
00:29:14.952	-0:08:42.36	0.060	716	109	1.59	47	-0.58	0.06	-3.08	0.28	-0.53	0.04
00:46:15.528	0:09:08.64	0.114	582	74	1.20	73	-0.81	0.11	-2.24	0.47	-0.94	0.06
00:47:20.400	-0:53:37.15	0.117	660	117	1.36	76	-0.52	0.06	-3.52	0.40	-0.46	0.04
00:56:00.120	0:37:56.74	0.067	557	81	1.23	50	-0.92	0.11	-3.76	0.43	-0.69	0.03
00:57:25.752	-0:31:12.00	0.044	465	40	1.06	38	-0.68	0.06	-1.96	0.18	-1.01	0.02
01:15:08.784	0:15:56.88	0.045	599	44	1.36	39	-0.56	0.05	-2.37	0.13	-0.70	0.03
01:16:39.816	0:37:25.68	0.044	601	48	1.37	37	-1.19	0.14	-3.42	0.36	-0.93	0.02
01:31:08.928	0:31:23.52	0.079	533	64	1.15	56	-0.70	0.08	-2.71	0.34	-0.73	0.04
01:34:49.824	-0:36:39.24	0.081	553	81	1.19	57	-0.75	0.10	-1.34	0.53	-0.98	0.11
01:37:25.704	-0:28:08.40	0.056	432	123	0.97	44	-1.13	0.21	-2.50	0.84	-1.20	0.08
02:02:15.600	-0:56:36.96	0.042	310	44	0.71	37	-1.10	0.09	-3.21	0.22	-0.93	0.01
03:06:17.376	-0:08:34.80	0.109	585	56	1.22	70	-0.64	0.07	-1.96	0.33	-0.84	0.06
03:26:23.232	-0:38:51.72	0.037	324	56	0.74	35	-1.08	0.13	-2.36	0.32	-1.26	0.01
10:07:55.441	0:35:29.04	0.097	493	49	1.04	64	-0.51	0.05	-1.86	0.23	-0.71	0.04
10:23:32.161	0:10:25.32	0.095	526	73	1.11	65	-0.73	0.19	-1.17	1.05	-1.17	0.12
10:49:15.839	0:57:15.84	0.106	474	78	0.99	68	-0.74	0.10	-1.67	0.43	-1.05	0.04
10:50:04.559	0:21:06.12	0.039	281	31	0.64	35	-1.07	0.13	-2.15	0.34	-1.35	0.02
12:46:54.240	0:18:31.32	0.089	844	89	1.80	62	-0.50	0.06	-2.46	0.28	-0.57	0.06
12:47:43.440	-0:09:07.20	0.088	994	102	2.13	61	-0.73	0.11	-2.94	0.48	-0.74	0.10
13:19:14.641	-0:53:58.20	0.083	704	73	1.52	58	-0.45	0.04	-3.44	0.16	-0.31	0.02
13:21:18.241	-0:44:19.32	0.108	873	131	1.82	70	-0.52	0.07	-2.85	0.33	-0.54	0.06
13:24:22.321	0:46:55.92	0.108	575	129	1.20	70	-1.06	0.14	-4.30	0.53	-0.76	0.04
13:45:05.760	0:13:55.20	0.089	284	43	0.61	62	-0.89	0.14	-2.86	0.55	-0.88	0.04
13:45:15.601	-0:08:30.84	0.088	362	42	0.77	64	-1.28	0.31	-3.50	1.19	-1.13	0.08
14:14:41.279	-0:24:20.44	0.137	761	80	1.52	81	-0.04	0.02	-2.00	0.17	-0.11	0.03
14:15:05.039	-0:29:08.16	0.141	930	113	1.85	84	-0.08	0.03	-2.07	0.23	-0.13	0.04
14:29:36.962	0:24:36.00	0.055	281	36	0.63	44	-1.05	0.15	-1.74	0.40	-1.48	0.04
15:08:31.919	-0:16:03.00	0.090	737	61	1.57	65	-0.42	0.05	-2.07	0.26	-0.54	0.05
15:11:19.918	-0:02:26.16	0.091	455	49	0.97	62	-0.58	0.06	-1.63	0.27	-0.76	0.07
15:16:23.522	0:06:09.00	0.119	675	120	1.39	76	-0.38	0.04	-1.24	0.34	-0.47	0.07
15:17:25.920	-0:38:24.36	0.116	758	92	1.56	77	-0.22	0.03	-2.94	0.21	-0.22	0.03
15:29:12.719	-0:15:07.92	0.087	459	54	0.98	63	-0.62	0.07	-2.52	0.27	-0.72	0.04

RA and DEC are both in J2000.0; z is the cluster redshift; σ_{cl} is the line-of-sight cluster velocity dispersion, as described in §2.3; $\Delta\sigma_{\text{cl}}$ is the bootstrap error on σ_{cl} ; R_{vir} is the virial radius of the cluster, as determined from Equation 1; V_{compl} is the completeness limit of the cluster GCVF, computed as described in §2.6; N_{200} and β and their errors, ΔN_{200} and $\Delta\beta$ are found by fitting Equation 16 to the cluster data; N'_{200} and the associated error, $\Delta N'_{200}$, is found by fitting Equation 16 while fixing β to its average value of -2.5.

inverse TFR, which converts from luminosity to circular velocity. Neither the TFR nor the inverse TFR have been calibrated in SDSS passbands. We therefore follow Sheth et al. (2003) in adopting the inverse I-band relation presented by Giovanelli et al. (1997) for 360 spiral galaxies deemed to be members of 24 clusters (their “in” sample). Although it was calibrated using cluster data, we applied the following relationship to late type galaxies in the determination of both the field and cluster GCVFs:

$$\log_{10}(2V_c) - 2.5 = -\frac{21.10}{7.94} - \frac{(M_I - 5 \log_{10} h_{100})}{7.94}, \quad (2)$$

where M_I is the k -corrected, extinction-corrected I-band absolute magnitude, extrapolated to infinity assuming an exponential surface brightness profile; and V_c is an estimate of the maximum rotational velocity of a galaxy. Although disk galaxy rotation curves exhibit a variety of shapes, the circular velocity generally increases with radius until it reaches a broad peak at ~ 10 kpc, beyond which it remains relatively constant. Thus V_c should be similar to the circular velocity measured at the flat part of the rotation curve.

In order to convert the observed SDSS magnitudes into those upon which the TFR is based, we first computed the r -band absolute total magnitude of each late type galaxy:

$$M_{r^*} = m_{r^*} - 5 \log d_L(z) + 5 - K(z), \quad (3)$$

where m_{r^*} is the apparent r -band Petrosian magnitude, d_L is the luminosity distance in parsecs, and $K(z)$ is the k -correction, computed using KCORRECT v1.11 (Blanton et al. 2003). We then use the conversion from Fukugita, Shimasaku & Ichikawa (1995) for late type galaxies: $M_{r^*} - M_I \sim 0.9$.

Internal extinction corrections were estimated using the procedure of Tully & Fouque (1985):

$$A = -2.5 \log \left[f (1 + e^{-a}) + (1 - 2f) \left(\frac{1 - e^{-a}}{a} \right) \right], \quad (4)$$

where $f = 0.1$ is the fraction of stars homogeneously mixed with a dust layer having opacity $\tau = 0.28$; $a = \tau \sec i$; and i is the inclination, estimated as:

$$\cos^2(i) = \frac{q^2 - q_0^2}{1 - q_0^2}. \quad (5)$$

Here $q_0 = 0.20$ is the intrinsic thickness and $q = \text{ab_exp}$ is the r -band axis ratio. The extinction is considered to be constant for $i > 80^\circ$.

The internal extinction corrections were on the order of ~ 0.5 magnitudes.

2.4.2 Early Type Galaxies

Early type galaxies occupy a thin plane in the space defined by stellar velocity dispersion, physical size, and surface brightness. Given the velocity dispersion and surface brightness, one can use the Fundamental Plane relation (FP; Djorgovski & Davis (1987); Dressler et al. (1987)) to estimate the size. In order to construct the GCVF from SDSS photometry, we require a relation that will yield the velocity dispersion (which is simply related to the circular velocity) given a size and surface brightness.

In a series of three papers (Bernardi et al. 2003,?,?), Bernardi and collaborators constructed a sample of ~ 9000 SDSS early type galaxies, from which they computed the joint distributions of σ_{los} , the line-of-sight velocity dispersion measured through a circular aperture with a radius equal to one-eighth the half-light radius ($r_0 = r_{\text{dev}}\sqrt{\text{ab_dev}}$); I_0 , the average surface brightness within r_0 ; and R_0 , the half-light radius in kpc. In order to determine the coefficients of the FP relation, Bernardi et al. (2003) used the above joint distributions to minimize the sum of $\Delta_1 = \log_{10} R_0 - a \log_{10} \sigma_{\text{los}} - b \log_{10} I_0 - c$ over all galaxies in their sample. In order to compute the coefficients for the inverse FP relation,

$$\log_{10} \sigma_{\text{los}} = a' \log_{10} R_0 + b' \log_{10} I_0 + c', \quad (6)$$

we used the same distributions to minimize the sum of $\Delta_{\text{invFP}}^2 = (\log_{10} \sigma_{\text{los}} - a' \log_{10} R_0 - b' \log_{10} I_0 - c')^2$ over all galaxies. We found $a' = 0.597$, $b' = -0.447$, and $c' = 5.449$.

For each early type galaxy, we estimated σ_{los} using Equation 6. Following Bernardi et al. (2003), we set

$$\mu_0 = M_{r^*} + 2.5 \log(2\pi r_0^2) - K(z) - 10 \log(1+z), \quad (7)$$

where $\mu_0 = -2.5 \log I_0$ and $K(z)$ is as previously defined.

In determining R_0 , the physical characteristic size, we first measured the angular characteristic size for each galaxy, r_0 . Because the inverse FP that we used was calibrated against galaxies at a variety of redshifts, the angular sizes measured in each band were linearly interpolated in order to determine the angular size at a rest wavelength corresponding to the central wavelength of each filter.

In order to plot early type galaxies on the same velocity scale as late types, we converted σ_{los} to V_c (see §2.4.1). Fitting non-parametric, spherical models to line profile and radial velocity dispersion data for 21 elliptical galaxies, Kronawitter et al. (2000) found that the circular velocity profiles of elliptical galaxies are flat to the 10 per cent level outside a radius of 0.3 effective radii. Gerhard et al. (2001) showed that there is a tight relation between the circular velocities in the flat regions of the rotation curves and the central velocity dispersions for these ellipticals. Ferrarese (2002) examined this relation, taking central velocity dispersions from Davies et al. (1987) for the ellipticals and correcting

them to an aperture of one-eighth the effective radius to find a relation between $\log_{10} V_c$ and $\log_{10} \sigma_{\text{los}}$. For an isothermal sphere, $V_c = \sqrt{2}\sigma_{\text{los}}$. Using the same data as Ferrarese (2002), we found that the isothermal assumption systematically underpredicts V_c , but that the data are consistent with the following relation:

$$V_c \approx 1.54\sigma_{\text{los}}. \quad (8)$$

For each observed early type galaxy, we use Equation 8 to determine V_c .

2.4.3 Accounting for Scatter in the Derived Circular Velocities

Values of V_c for individual galaxies were computed with the mean relations in §2.4.2 and §2.4.1. Sheth et al. (2003) note that if the scatter is significant, the use of mean relations can significantly distort the shape of the GCVF. Therefore, in constructing our GCVFs, we accounted for the scatter by representing each galaxy's V_c as a probability distribution, rather than a single value. Because we calculated V_c using different relations for early and late type galaxies, this distribution depends on galaxy type.

The circular velocities for late type galaxies were computed directly from the inverse TFR (§2.4.1). We therefore adopted the model for the scatter around V_c provided by Giovanelli et al. (1997).

$$\langle \Delta_{\text{invTF}}^2 \rangle = \frac{(-0.28(\log_{10}(2V_c) - 2.5) + 0.26)^2}{63.04}. \quad (9)$$

The circular velocities for early type galaxies were computed using Equations 6 and 8. There were two sources of scatter in determining V_c : the scatter around σ_{los} and the uncertainty in the relationship between σ_{los} and V_c . We estimated the former by exchanging V and R in the expression for $\langle \Delta_1^2 \rangle$ in Equation 4 of Bernardi et al. (2003) and using the joint distributions of σ_{los} , R_0 , and I_0 presented in their Table 1. Doing so yielded a scatter of $\langle \Delta_{\text{invFP}}^2 \rangle = 0.061$ in $\log_{10} \sigma_{\text{los}}$. Sheth et al. (2003) found that the scatter in $\log_{10} \sigma_{\text{los}}$ depends slightly on $\log_{10} \sigma_{\text{los}}$. This was a small effect compared to our other sources of error; we therefore treated the scatter in the Fundamental Plane as constant. The conversion from σ_{los} to V_c (Equation 8) was calibrated on only ~ 20 elliptical galaxies. Therefore a robust model of the scatter due to this conversion was not possible and we neglected it.

Because the Fundamental Plane and Tully-Fisher relations were calibrated using samples created under more stringent selection criteria than we used, the above relations underestimate the scatter that exists in our data.

2.5 Background Subtraction

The largest uncertainty in our determinations of cluster GCVFs stemmed from the difficulty in determining cluster membership. Because a spectrum is not available for every galaxy in the field of each cluster, our background subtraction is statistical. We calculated the circular velocity for every galaxy within the virial radius of each cluster under the assumption that it lies at the cluster redshift. Clearly, some galaxies have redshifts greater or less than that of the cluster, and our calculations were incorrect for these

galaxies. This effect was removed during our background subtraction procedure. Again using the cluster redshift, we calculated the circular velocity for every galaxy within an annulus bounded by inner and outer radii of 3 and 5 Mpc, respectively. These galaxies should have a redshift distribution similar to that of the cluster interlopers. Thus, by subtracting the appropriately normalized GCVF of galaxies in the annulus, we corrected for the interlopers.

The error in the number of galaxies in each circular velocity bin are calculated assuming Poisson noise in both the total counts within the virial radius, C_{tot} , and the counts within the background annulus, $C_{\text{background}}$:

$$\sigma_N^2 = C_{\text{tot}} + f^2 C_{\text{background}}, \quad (10)$$

where f is the normalization factor applied to the background annulus counts to account for the difference in its area and that of the virialized part of the cluster ($0.02 \lesssim f \lesssim 0.3$).

The contribution to the total error in the GCVFs from the Poisson error in the background counts decreases with increasing V_c . Above $\sim 200 \text{ km s}^{-1}$, the contribution is less than 40 per cent.

2.6 Completeness

Because our procedure distinguishes between morphological types, we could assign different values of V_c to galaxies of the same luminosity. Our requirement that $r^* < 21.5$ therefore leads to a cut in V_c that depends on both redshift and galaxy type. Figure 1 illustrates the effect our magnitude limit has on V_c for a representative cluster. The filled points represent early type galaxies, while the hollow points represent late type galaxies. For this cluster, 90 per cent of galaxies with $21 < r^* < 21.5$ have $V_c > 83 \text{ km s}^{-1}$. Below this completeness velocity, V_{compl} , significant numbers of galaxies are missing from our sample. All GCVFs in what follows are truncated below V_{compl} , which was calculated independently for each cluster. The adopted values are listed in Table 1, column 7.

3 METHODS: SIMULATIONS

In order to compare our observational results against simulations, we compiled a set of 15 simulations of the dark matter components of clusters. Each simulated cluster was evolved in the currently favored Λ CDM cosmology with $\Lambda=0.7$, $H_0 = 70 \text{ km s}^{-1} \text{ Mpc}^{-1}$, $\Omega_0 = 0.3$, and $\sigma_8 = 1$. Ten are the most massive clusters from the zero redshift output of the $50^3 h_{100}^{-3} \text{ Mpc}^3$ simulation described in Reed et al. (2003). This simulation has a particle mass of $1.9 \times 10^8 M_\odot$ and a force resolution of 7.14 kpc. An additional four clusters were simulated using the volume renormalization technique (Katz & White 1993) and have $(0.5-0.9) \times 10^5$ particles within the virial radius and force softenings of $\lesssim 1$ per cent of the virial radius. Further details on these four simulations can be found in Borgani et al. (2002).

The 14 cluster simulations were of sufficient resolution to robustly determine peak circular velocities in subhalos above the completeness velocities of our observed GCVFs (see §2.6). They were of insufficient resolution, however, to accurately trace subhalo internal density profiles. These were necessary to determine the effects of baryons on galaxy

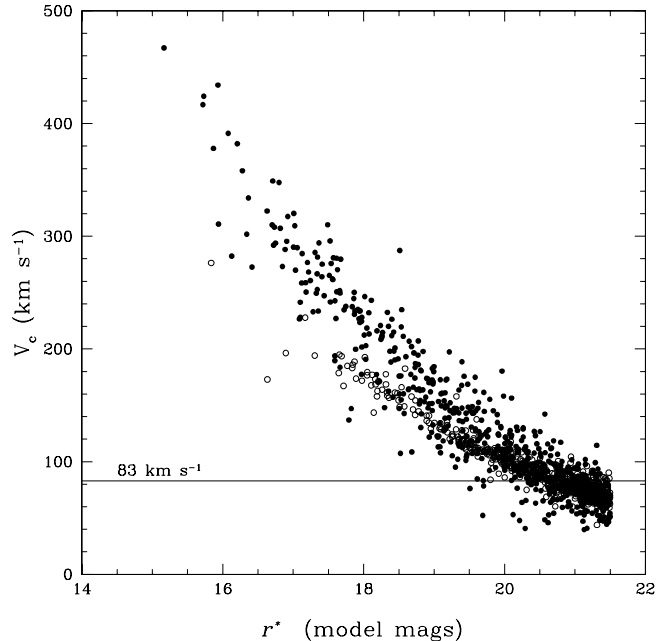


Figure 1. Illustration of the completeness limit for one cluster in our sample. Each point represents a galaxy within R_{vir} for a representative cluster in our SDSS sample. No background subtraction has been carried out. Filled circles are early type galaxies, and hollow circles denote late type galaxies. Ninety per cent of all galaxies with $21 > r^* > 21.5$ lie below the completeness velocity of $V_{\text{compl}} = 83 \text{ km s}^{-1}$ for this cluster.

Table 2. Simulation Sample

	σ_{cl} km s^{-1}	M_{200} $10^{13} M_\odot$	R_{200} $h_{70} \text{ Mpc}$	m_{DM} $10^8 M_\odot$	N_{DM} 10^6	ϵ kpc
Box01	525	29.4	1.73	1.9	1.5	7.14
Box02	458	26.6	1.67	1.9	1.4	7.14
Box03	383	21.7	1.56	1.9	1.1	7.14
Box04	456	18.4	1.48	1.9	0.97	7.14
Box05	451	17.9	1.46	1.9	0.94	7.14
Box06	342	15.4	1.39	1.9	0.81	7.14
Box07	388	13.0	1.32	1.9	0.68	7.14
Box08	332	11.6	1.27	1.9	0.61	7.14
Box08	369	10.3	1.22	1.9	0.54	7.14
Box10	366	8.9	1.26	1.9	0.47	7.14
Hickson	234	2.5	0.76	4.41	0.0486	2.5
Fornax	400	5.9	0.65	4.41	0.118	2.5
Virgo	565	30.4	1.75	14.9	0.179	1.25
Coma	1007	133.6	2.86	119.2	0.090	3.75
HR Virgo	600	30	1.75	3	1.00	1.25

Further details on the simulated clusters named Box01 – Box10 can be found in Reed et al. (2003). The simulations labelled Hickson, Fornax, Virgo, and Coma are described in Borgani et al. (2002). The last is used in §4.4. *Columns:* σ_{cl} is the velocity dispersion of the simulated cluster, R_{200} is the radius within which the average density is 200 times the critical density, M_{200} is the mass within R_{200} , m_{DM} is the mass of each dark matter particle, N_{DM} is the number of dark matter particles within R_{200} , and ϵ is the force softening.

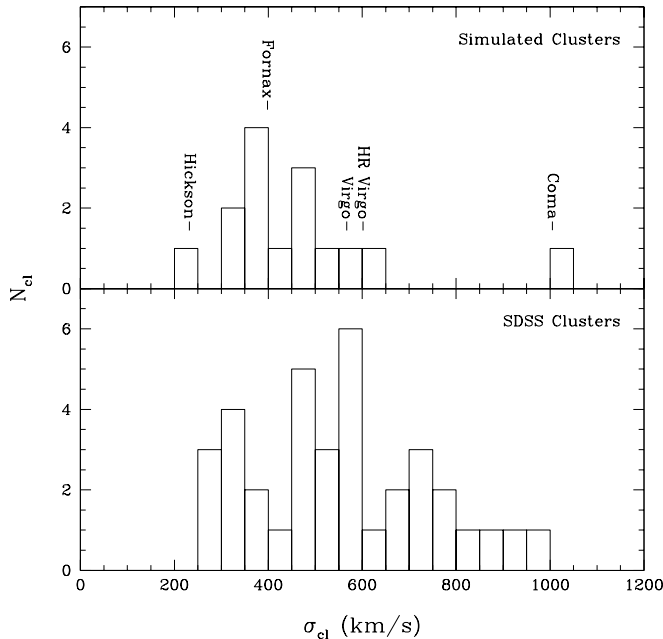


Figure 2. *Top Panel:* The distribution of cluster velocity dispersions for the fifteen simulations described in §3. *Bottom Panel:* The distribution of cluster velocity dispersions, calculated by the methods described in §2.3, for our sample of 34 SDSS clusters.

rotation curves, as we describe in §4.4. For this purpose, we used a very high resolution N -body simulation of a galaxy cluster with $\sigma_{\text{cl}} = 600 \text{ km s}^{-1}$ and $M_{\text{vir}} = 3 \times 10^{14} M_{\odot}$, represented by approximately one million particles within $R_{\text{vir}} = 1.75 \text{ Mpc}$. It was evolved in a 100^3 Mpc^3 volume where the force spline softening was 1.25 kpc and the large scale structure was sampled at a lower resolution.

Subhalos were identified using SKID (Stadel 2001; Governato et al. 1997), a halo finder based on local density maxima and particularly suited to finding subhalos within larger structures. Peak circular velocities were also output by SKID. We used *Tipsy*² to extract full density profiles from our highest resolution simulation.

4 RESULTS

4.1 The Shape of the GCVF

A Press-Schechter mass function combined with $M \propto V^3$ and a value of $n = 2$ for the fluctuation-spectrum index give

$$\frac{dN(V_{\text{pk}})}{dV_{\text{pk}}} \propto V_{\text{pk}}^{-4}. \quad (11)$$

Moore et al. (1999) and Ghigna et al. (2000) found the GCVF in high resolution simulations of a Virgo-like cluster to be consistent with the above power law. Moore et al. (1999) also found the observed GCVF of Virgo to be consistent with it. In Figure 3 we plot the GCVFs for our sample of 34 clusters in three cluster velocity dispersion bins. The bins were chosen such that each contains approximately the

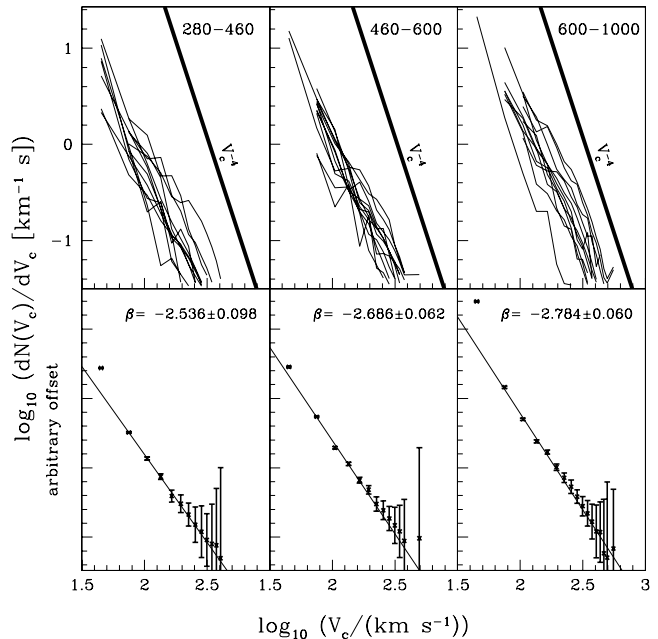


Figure 3. The observed CGVF, binned by cluster velocity dispersion. *Top panels:* Individual cluster GCVFs are shown with thin lines. The dark line in each panel has a slope of -4, and is provided for reference. Cluster velocity dispersion ranges are shown in the upper right of each panel, in km s^{-1} . *Bottom panels:* Each panel shows the composite functions constructed from clusters having σ_{cl} in the range indicated in the panel directly above. Error bars take into account Poisson error in counting galaxies both within R_{vir} and in the background annulus. A power law (Equation 16) was fitted to these data, and is shown as a thin solid line. The slopes of the composite functions are shown in the upper right hand corner of each panel.

same number of clusters. The bold lines have a slope of -4 and are for reference only. From this figure, we can see that the observed cluster GCVF is a power law. The power law form of the cluster GCVF, while predicted analytically and numerically, is nonetheless somewhat surprising. The cluster luminosity function is usually described by a Schechter function. Because the luminosities of both early and late type galaxies are related to their circular velocities by power laws ($L \propto V^n$), it is not obvious that the galaxy population as a whole should obey both a Schechter luminosity function and a power law GCVF.

Key to the explanation is the fact that both early and late types contribute to the GCVF, and that they have both different relations between M_{r^*} and V_c , and make up different fractions of the population with magnitude. Because the slope of the $V_c - M_r$ relation for early types is steeper than for late types, late type galaxies were mapped onto a smaller range of velocities than early types. Thus, late type galaxies that populate the knee in the luminosity function were mapped to lower velocities than early type galaxies with the same luminosity. The proportion of early and late type galaxies that make up the knee in the luminosity function affects the placement and prominence of the knee in the GCVF. In general, it was smeared out in the GCVF. This is the main reason that our observed cluster GCVFs

² <http://www-hpcc.astro.washington.edu/tools/tipsy/tipsy.html>

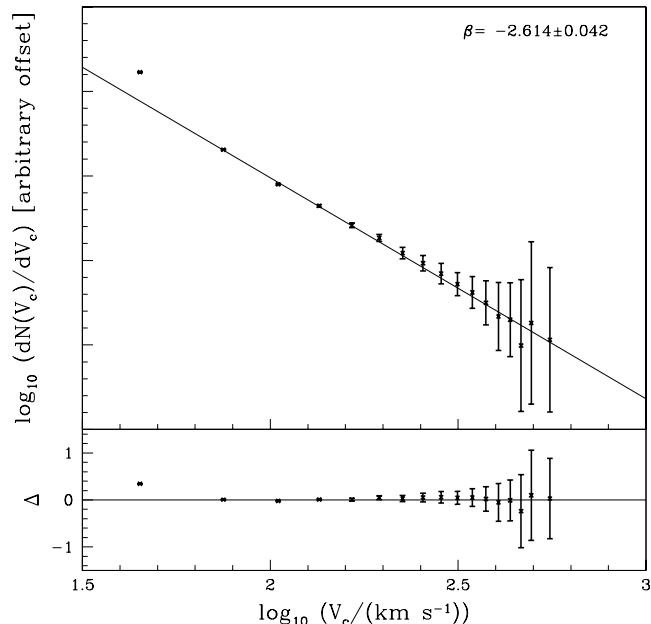


Figure 4. The composite CGVF, constructed from all 34 SDSS clusters in our sample. *Top panel:* The error bars were computed as in Figure 3. The best-fitting power law is shown as a thin solid line, and its slope is shown in the upper right hand corner. *Bottom panel:* The residuals of the composite cluster GCVF from the best fit power law. The power law is a very good fit to the composite GCVF, except for the lowest V_c bin.

look like power laws. If a single luminosity-velocity relation is used to compute a GCVF from a population of galaxies drawn from a Schechter function, the resulting GCVF will also be a Schechter function (Cole & Kaiser 1989). If two different luminosity-velocity relations are used in the computation, it is still possible to arrive at a Schechter GCVF, as found by Gonzalez et al. (2000) and Kochanek & White (2001). A Schechter GCVF will not *necessarily* result, however, depending upon the relative abundances of early and late type galaxies as a function of luminosity.

Another reason for the power law GCVF is that our completeness limits did not allow us to observe the shape of the GCVF at velocities dominated solely by galaxies from the flat part of the luminosity function, where we would expect the GCVF to flatten out. Thus, very few bins define the knee.

Finally, the signal-to-noise in each cluster GCVF is relatively low due to the small number of galaxies used. It would be difficult to trace the high velocity exponential drop-off if the GCVF did follow a Schechter function.

In order to increase the signal to noise in our determination of the cluster GCVF, we built composite cluster GCVFs using a technique analogous to that of Colless (1989) for building composite cluster luminosity functions. The number of galaxies in the j th V_c bin of the composite cluster GCVF is given by:

$$N_{cj} = \frac{N_{c0}}{m_j} \sum_i \frac{N_{ij}}{N_{i0}}, \quad (12)$$

where N_{ij} is the number of galaxies in the j th bin of the i th cluster GCVF, N_{i0} is the normalization used for the i th cluster GCVF (taken as the number of galaxies brighter than 100 km s^{-1}), m_j is the number of clusters contributing to the j th bin, and N_{c0} is the sum of all the normalizations:

$$N_{c0} = \sum_i N_{i0}. \quad (13)$$

The error on N_{cj} is:

$$\Delta N_{cj} = \frac{N_{c0}}{m_j} \left[\sum_i \left(\frac{\Delta N_{ij}}{N_{i0}} \right)^2 \right]^{\frac{1}{2}}, \quad (14)$$

where ΔN_{ij} is the error on the j th bin of the i th cluster.

The composite cluster GCVFs in the three σ_{cl} bins are shown in the bottom panel of Figure 3. The composite cluster GCVF constructed using all 34 clusters is shown in Figure 4. An increase in signal to noise still yielded a power law form.

4.2 Is cluster substructure self-similar?

Moore et al. (1999) found that the cumulative GCVF for a Virgo-like simulation is identical to that of subhalos within a Milky-Way-like simulation, provided the velocities are scaled by the velocity of the parent halo ($V_{cl} = \sqrt{2}\sigma_{cl}$). In the top panel of Figure 5, we have plotted the cumulative, scaled GCVF for all fifteen simulated clusters from Table 2. Our simulated clusters have very similar cumulative, scaled GCVFs, in agreement with the results of Moore et al. (1999).

In the bottom panel of Figure 5, we plot the same quantity for our sample of SDSS clusters. The slopes and offsets of the simulated and observed clusters cannot be compared directly, since the effects of baryons have not been included in the simulations. However, assuming that baryonic physics changes the shapes of all the GCVFs in a similar way, we can compare the scatter in the observed and simulated GCVFs. The observations display a significantly larger scatter than the simulations. Uncertainties in the measurement of V_{cl} and Poisson errors both contribute to the observed scatter. Taking the plot of $\log_{10}[N(> (V_c/V_{cl}))]$ versus V_c/V_{cl} to be a power law, the variance in $\log_{10}[N(> (V_c/V_{cl}))]$ due to measurement errors in σ_{cl} is

$$\Delta_{\log_{10}[N(>(V_c/V_{cl}))]}^2 = \frac{1}{\ln 10} \frac{\Delta_{V_{cl}}^2}{V_{cl}^2}, \quad (15)$$

where $V_{cl} = \sqrt{2}\sigma_{cl}$. Using the values of σ_{cl} found in §2.3, and computing $\Delta_{V_{cl}}$ from the errors in σ_{cl} , we found that the scatter due to measurement errors in σ_{cl} is 0.009, while the scatter due to Poisson noise is 0.012. The total observed scatter is 0.064. Thus, the intrinsic scatter is ~ 0.043 . This is very similar to the intrinsic scatter we measured in the simulations. Thus our observed GCVFs show the same degree of variations found in Λ CDM dark matter cluster simulations.

4.3 Trends in the Cluster GCVF with Cluster Velocity Dispersion

Figure 3 shows that the cluster GCVF depends upon the cluster velocity dispersion. To quantify the observed cluster

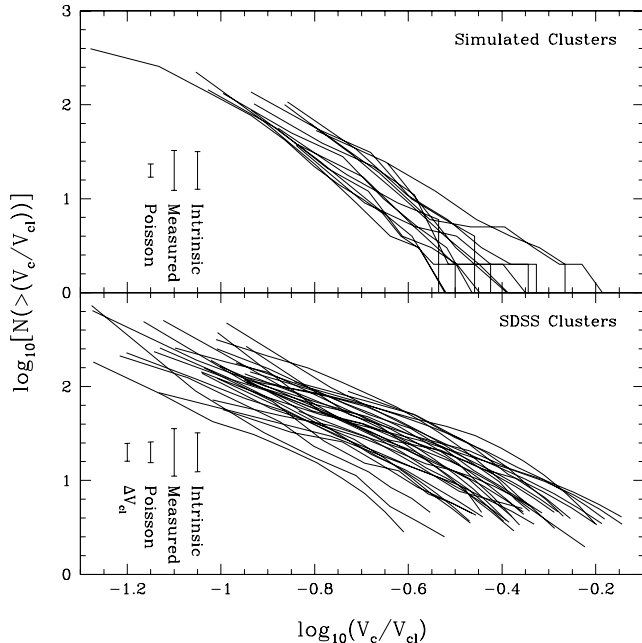


Figure 5. The simulated and observed SDSS CGVFs, with galaxy circular velocities scaled by cluster circular velocities. The error bars have length 2Δ , where Δ is the RMS scatter at $\log_{10}(V_c/V_{cl}) \approx -0.7$ due to various sources, as labelled. *Poisson* refers to Poisson noise in counting galaxies within R_{vir} for the simulated clusters and to Poisson noise in counting galaxies within R_{vir} and the background annulus for the SDSS clusters. *Measured* refers to the total measured scatter. ΔV_{cl} refers to the scatter in $\log_{10}[N(>(V_c/V_{cl}))]$ due to errors in measuring V_{cl} , and *Intrinsic* refers to the portion of the total measured scatter unaccounted for by Poisson scatter in the case of the simulations or by both Poisson scatter and that induced by ΔV_{cl} for the SDSS clusters.

GCVF and its dependence on σ_{cl} , we fitted each with a function of the following form:

$$\log \left[\frac{dN(V_c)}{dV_c} \right] = \log_{10} N_{200} + \beta \log_{10} \left(\frac{V_c}{200 \text{ km s}^{-1}} \right), \quad (16)$$

where β represents the slope of the power law and N_{200} is the normalization at $V_c=200 \text{ km s}^{-1}$. The results of the fit are reported in Table 1, columns 8–11, and are plotted against $\log_{10} \sigma_{cl}$ in Figure 6 (filled points). The top panel of Figure 6 shows that the slope, β , while showing a fair amount of scatter, does not vary systematically with σ_{cl} . It has a mean value of $\bar{\beta} = -2.5 \pm 0.8$. The slope of the composite cluster GCVF shown in Figure 4 is -2.61 ± 0.04 , consistent with the mean slope. The normalizations of the individual cluster GCVFs are plotted in the middle panel of Figure 6 and show a clear systematic trend in the sense that higher mass clusters host more galaxies. The best fit line to these data are

$$\log_{10} N_{200} = (2.26 \pm 0.2) \log_{10} \sigma_{cl} - (6.84 \pm 0.6). \quad (17)$$

Finally, we recalculated our normalizations with the slope fixed to its mean value of -2.5 . These values of N'_{200} can be found in Table 1, columns 12 and 13, and are plotted against σ_{cl} in the third panel of Figure 6. The best fit line to these data are

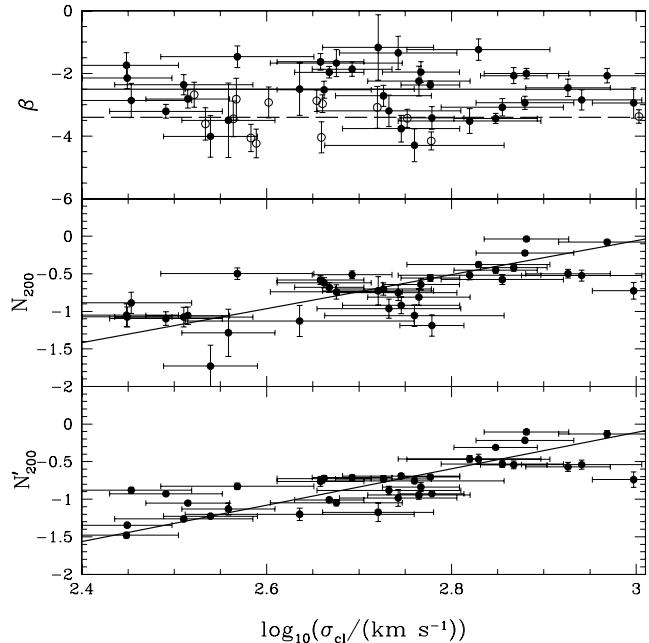


Figure 6. Each observed and simulated cluster GCVF was fit to the equation $\log_{10} dN/dV_c = \log_{10} N_{200} + \beta \log_{10} (V_c/200 \text{ km s}^{-1})$. *Top Panel:* The slope of the cluster GCVF as a function of cluster velocity dispersion. Solid points are for the observed cluster GCVFs. The mean value is indicated by the solid line. Open points are for the simulated cluster GCVFs. The mean value is indicated by a dashed line. *Middle Panel:* The normalization of the observed cluster GCVF as a function of cluster velocity dispersion. High σ_{cl} clusters tend to contain more galaxies than low σ_{cl} . The line that best fits this trend is given by Equation 17 and is overplotted. *Bottom Panel:* The normalizations of the fits for the observed cluster GCVFs were recomputed while holding the slope fixed to the mean value shown in the top panel. The new normalizations are plotted against σ_{cl} in the bottom panel. The line that best fits these data is given by Equation 18 and is overplotted.

$$\log_{10} N'_{200} = (2.42 \pm 0.2) \log_{10} \sigma_{cl} - (7.37 \pm 0.5). \quad (18)$$

This slope is somewhat smaller than theoretically expected, but not at a statistically significant level.

We compared the slopes of the observed GCVFs to those of the simulated GCVFs. The latter are plotted as open circles in the top panel of Figure 6. The dashed line is drawn at their mean value: $\bar{\beta}_{sim} = -3.4 \pm 0.8$. The average value of the simulations is somewhat steeper than that of the observations, although formally they agree within the uncertainties. It should be noted that the slopes are not directly comparable because the simulations do not account for the effects of baryons. The effects of baryons on the slope of the GCVF are discussed in the next subsection.

4.4 The Effects of Baryons on the Cluster GCVF

We found in §4.3 that subhalos in simulated clusters have steeper GCVFs than measured for galaxies in clusters. We also noted that a more meaningful comparison between observations and simulations would require a determination of the circular velocity profile taking into account the effects

of both dark matter *and* baryons. Baryons affect the circular velocity profile of a galaxy in two ways. First, they significantly contribute to the enclosed mass at small radii. Second, they adiabatically pull the dark matter into a more concentrated equilibrium configuration than it would have in their absence. The total circular velocity profile is therefore given by

$$V_c^2(r) = V_{c,b}^2(r) + V_{c,DM}^2(r), \quad (19)$$

where $V_{c,b}(r)$ is the circular velocity profile of the collapsed baryonic mass and $V_{c,DM}(r)$ is the circular velocity profile of the adiabatically contracted dark matter halo.

The degree of these effects depends on the mass distribution of the baryons. The challenge lies in populating the subhalos with galaxies in a way that mimics, as closely as possible, observed empirical relations. A full description of the baryonic mass distribution requires knowledge not only the density profile shape (galaxy type), but also a normalization (total galaxy mass) and a scalelength (galaxy size). Our method for populating the subhalos identified in our highest resolution simulation is described in Appendix A. Given the density profiles of the baryonic component of each subhalo, their circular velocity profiles were computed. Hernquist profiles are spherical, so the rotation curves of early type galaxies were straightforward to calculate: $V_{sph} = GM(r)/r$. Determining the rotation curve of exponential profiles was also straightforward, but required taking account of the non-spherical geometry.

The determination of $V_{c,DM}(r)$ required modelling how the dark matter responds to the collapse of the baryons. We assumed that the baryons contract slowly and that the halo remains spherical. Under these conditions, a dark matter particle conserves angular momentum as it moves closer to the center of the potential (Blumenthal et al. 1986; Dalcanton et al. 1997; Mo, Mao & White 1998):

$$M_f(r_f)r_f = M_i(r_i)r_i, \quad (20)$$

where r_i is the initial mean radius of the particle, r_f is the final mean radius of the particle, and

$$M_f(r_f) = M_b(r_f) + M(r_i)(1 - f_{cool}). \quad (21)$$

Equations 20 and 21 both require knowledge of $M(r_i)$, the initial mass profile of the dark matter halo, before adiabatic contraction. While V_{pk} was robustly measured from all of the simulations listed in Table 2, a reliable determination of $V(r_i)$ or $M(r_i)$ could only be made from the simulation described by the last entry in Table 2, which has both very high resolution and a small softening scale. Using the measured $M(r_i)$, the values of f_{cool} described in §A0.2, and the $M_b(r)$ computed from the density profiles described in Appendix A, we calculated $M(r_f)$ from Equations 20 and 21. From $M(r_f)$ it was trivial to calculate $V_{c,DM}(r)$.

Once the total circular velocity profile $V_c(r)$ due to dark matter and baryons was determined, we measured a characteristic circular velocity, V_c , that is analogous to that deduced for our observed early and late type galaxies. We estimated V_c as the circular velocity at three scale lengths.

In Figure 7, we compare the simulated GCVF to that of SDSS clusters that have similar velocity dispersions. The dashed line represents the simulated cluster GCVF in the limit of no baryons and assuming that $V_c = V_{pk}$. The simulated cluster GCVF in this case is too steep, underpredict-

ing the number of galaxies at high V_c . The bold solid lines bracket simulated GCVFs which have been corrected for the effects of baryonic infall. We varied the total mass that infalls to form ellipticals ($0.025 < f_{cool} < 0.1$) and the peak circular velocity above which subhalos host early type rather than late type galaxies ($125 \text{ km s}^{-1} < V_{break} < 150 \text{ km s}^{-1}$). See Appendix A. When the effects of baryons were included, the number of high V_c galaxies increased, while the number of low V_c galaxies decreased, bringing the simulations into rough agreement with the observations. This effect held whether V_c was measured at 2, 3, or 4 scale lengths, but was strongest if V_c was measured at 2 scale lengths.

While Λ CDM models can reproduce the cluster GCVF, they overproduce the number of field galaxies with $V \lesssim 120 \text{ km s}^{-1}$ (Gonzalez et al. 2000; Kochanek & White 2001). Any solution to the disagreement in the field must preserve the agreement found in clusters. Modifications to CDM would affect the substructure within clusters as well as in the field, and tend to contradict other observations (Barkana, Haiman & Ostriker 2001; Gnedin & Ostriker 2001; Hui 2001; Miralda-Escudé 2002). Supernova feedback alone fails to reproduce the luminosity function of the Local Group (Somerville 2002), but a combination of feedback and squelching can. However, squelching cannot play a role at the circular velocities we have investigated here. It affects only galaxies with circular velocities $\lesssim 50 \text{ km s}^{-1}$. The importance of supernova feedback at higher circular velocities is uncertain. Recent work by Mac Low & Ferrara (1999) suggests that it can only regulate star formation, not remove mass at these scales. Regardless, it should be equally important in clusters and in the field. Finally, any incompleteness that exists in our cluster GCVF should also exist in our field GCVF.

4.5 The Cluster Versus Field GCVF

The circular velocity function of dark matter halos within clusters is expected to be a function of environment. Although we found only small differences among the populations of massive clusters, there may still be substantial differences between clusters and the field. First, hierarchical clustering theory predicts that massive halos form from rarer density peaks and should therefore be more clustered than low mass halos (Kaiser 1984; Davis et al. 1985; White et al. 1987, 1988; Governato et al. 1998). Second, halos within clusters are subject to the mass-altering processes of tidal stripping, dynamical friction, and galaxy harassment (Moore et al. 1996). Third, low mass halos in dense regions formed, on average, earlier than those in the field. Reionization can therefore preferentially suppress the late-time formation of galaxies within low mass halos in the field (Quinn, Katz & Efstathiou 1996; Tully et al. 2002; Benson et al. 2002; Somerville 2002), although at velocities below what we can probe in this work.

Cole & Kaiser (1989) determined the circular velocity function of field galaxies by starting with a Schechter luminosity function and assuming $L \propto V_c^{3-4}$, not taking into account that a late type galaxy has a lower circular velocity than an early type with the same absolute magnitude, or that their relative abundances depend upon luminosity. Shimasaku (1993) computed the field GCVF galaxy-by-galaxy using both HI 21 cm line widths (~ 400) and the

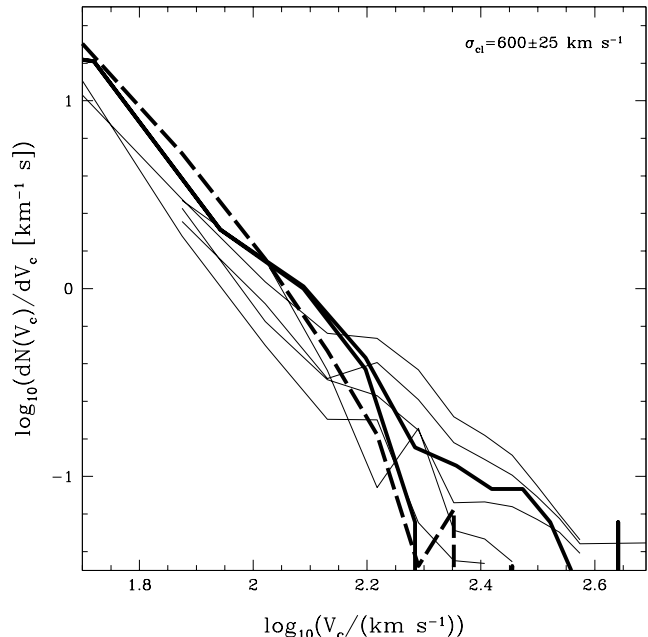


Figure 7. Comparison of the GCVF measured from our highest resolution galaxy cluster simulation (HR Virgo) to that measured in SDSS clusters. The dashed line is the simulated GCVF constructed using the V_{pk} values output by SKID. Thick solid lines represent the range of corrected GCVFs given uncertainties in how gas infall affects galaxy rotation curves (see Appendix A for details). Thin solid lines are the GCVFs of SDSS clusters with measured velocity dispersions within 25 km s^{-1} of that of the simulated cluster.

Tully-Fisher relation (~ 300) for spiral galaxies and stellar velocity dispersions (~ 100) and the Faber Jackson relation (~ 90) for early type galaxies. They found that early types dominate at the high velocity end.

Gonzalez et al. (2000) determined the field GCVF by performing variable transformations on the type-specific B-band luminosity functions determined from the SSRS2 survey. They found that, given the available Tully-Fisher and Faber Jackson Relations, all field galaxies could be treated as late types without changing the results. Doing so, they found that the number density of galaxies per unit velocity can be described by a Schechter function,

$$\tilde{\Psi}(V_c)dV_c = \tilde{\Psi}_* \left(\frac{V_c}{V_{c,*}} \right)^\beta \exp \left[- \left(\frac{V_c}{V_{c,*}} \right)^n \right] \frac{dV_c}{V_{c,*}}, \quad (22)$$

where $\tilde{\Psi}_* = (3.2 \pm 0.6) \times 10^{-2} \text{ Mpc}^{-3} h^3$, $\beta = -1.3 \pm 0.13$, $n = 2.5$, $V_{c,*} = 247 \pm 7$. Kochanek & White (2001) found similar results, although they took into account the different transformations for early and late types. Sheth et al. (2003) analyzed field early type galaxies within the SDSS, and found that accounting for the scatter around the mean Tully-Fisher and Faber Jackson or Fundamental Plane relations is extremely important for reproducing the high velocity end of the GCVF.

In order to allow a direct comparison to our cluster GCVFs, we constructed a field GCVF using the same relations that we used in the previous cluster analysis. We select galaxies from the SDSS EDR spectroscopic sample with

$14.5 > r^* > 17.77$. Each of the resulting $\sim 29,000$ galaxies was assigned a weight equal to the inverse of the volume over which the galaxy could be observed, given the apparent magnitude limits. Circular velocities were computed for each galaxy as described in §2.4.1 and §2.4.2. The scatter was dealt with as described in §2.4.3. The value of the field GCVF in a given circular velocity bin is equal to the sum of the weights of the galaxies in that bin. The results are plotted as points with error bars in Figure 8, along with the functional forms for the field GCVF given by Gonzalez et al. (2000) (Equation 22; solid bold line). Figure 8 illustrates that the cluster GCVF shows much less curvature than that of the field, being steeper for $V_c \lesssim 200 \text{ km s}^{-1}$ and more shallow for $V_c \gtrsim 200 \text{ km s}^{-1}$.

Following the discussion in Section 4.3, the difference in the shapes of the field and cluster GCVFs can be explained by their different relative abundances of early and late type galaxies as a function of luminosity. It must be noted that our division of galaxies into early and late types depends upon the $u^* - r^*$ color, which is sensitive to star formation. There is some evidence that the cluster environment suppresses star formation (Couch et al. 1987; Barger et al. 1996; Poggianti et al. 1999). A field galaxy that falls into a cluster and experiences truncated star formation would redden, but its r^* -band luminosity would not change significantly, because r^* is sensitive to the total stellar mass. If the change in $u^* - r^*$ is large enough to change late types into early types, the cluster GCVF would have more high-velocity galaxies and fewer lower-velocity galaxies relative to the field, as is observed. While the trend is correct, detailed models are required to determine to what extent this effect can explain the observed differences between the field and cluster GCVFs.

5 SUMMARY

We constructed the cluster and field galaxy circular velocity functions using data from the Sloan Digital Sky Survey Early Data Release. Circular velocities were determined using the inverse Tully-Fisher and Fundamental Plane relations on a galaxy-by-galaxy basis, rather than by performing a transformation of variables on a functional fit to the luminosity function. For comparison to the observations, we also analyzed the GCVFs determined from 15 clusters simulated in the Λ CDM concordance cosmology. Our results can be summarized as follows:

1. We found that, although the observed cluster luminosity function is a Schechter function, the observed cluster GCVF can be described as a power law.
2. We tested the self-similarity claimed by Moore et al. (1999) for our scaled simulated and observed cluster GCVFs. The simulated GCVFs are indeed very similar to one another, and show only a small scatter. The scatter in the observed cluster GCVFs is much larger, but can be explained by measurement error. Thus, the intrinsic scatter in the observed cluster GCVF is similar to that predicted.
3. The normalization of the observed cluster GCVF increases with cluster velocity dispersion, while the slope is constant. The average slope of the observed cluster GCVF is somewhat flatter ($\beta \approx -2.5$) than that computed from Λ CDM cluster simulations ($\beta = -3.4$). However, the errors

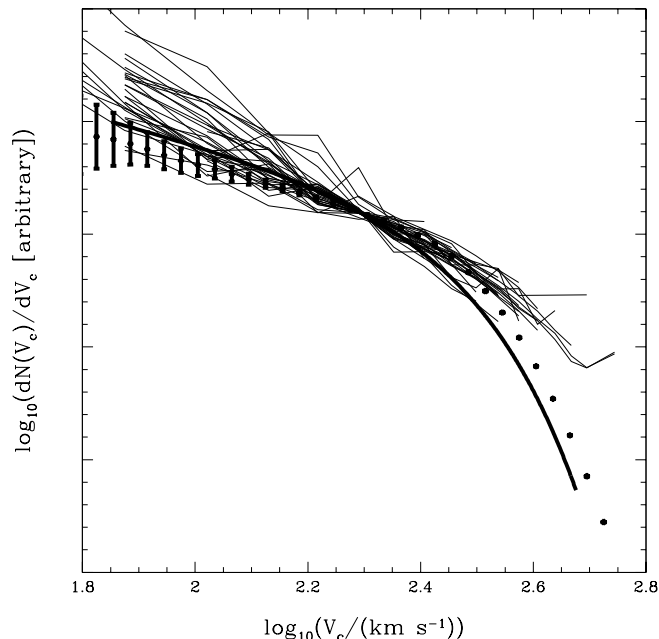


Figure 8. GCVFs for the SDSS cluster sample and the field. The thin lines represent the GCVFs for SDSS clusters, normalized at $\log_{10}(V_c / \text{km s}^{-1}) \approx 2.3$. The solid bold line is the similarly normalized observed field GCVF as determined by Gonzalez et al. (2000). The points with error bars are the field GCVF determined from SDSS data as described in §4.5. Because of the arbitrary normalization, this plot is suitable only for assessing differences in the shape of the GCVF in clusters and the field. Although the cluster GCVFs display a range of slopes, they are steeper than the field for $V_c \lesssim 200$ and more shallow for $V_c \gtrsim 200$. The field GCVFs are consistent with one another within the error bars at $V_c < 200 \text{ km s}^{-1}$. The field GCVF we determined lies above that measured by Gonzalez et al. (2000) at $V_c > 200 \text{ km s}^{-1}$ because we took into account the scatter around the relations used to compute V_c for early type galaxies, which dominate the GCVF at large V_c .

on these average slopes are large, and overlap. If the difference between the simulated and the observed clusters is real, it is most likely due to the fact that the simulations do not include the effects of baryons on galaxy rotation curves.

4. We estimated the effects of baryons on the simulated GCVFs. Baryons can flatten the simulated GCVF enough to bring it into agreement with the GCVFs of observed clusters with similar velocity dispersions. This agreement between the amount of cluster substructure predicted by N-body simulations and that observed in real clusters has been found previously by Moore et al. (1999) for an SCDM simulation of a Virgo-like cluster. Our approach is different in that we treat early and late types distinctly, as well as account for the effects of baryons on galaxy rotation curves. In addition, our simulated cluster has evolved in the concordance cosmology.

ACKNOWLEDGMENTS

VD and DR acknowledge funding from the Graduate Student Researchers Program.

JJD was partially supported through the Alfred P. Sloan Foundation.

TRQ was partially supported by the National Science Foundation.

Simulations were run at the ARSC (Fairbanks) and CINECA (Bologna, Italy) supercomputing centers.

This research has made use of the NASA/IPAC Extragalactic Database (NED), which is operated by the Jet Propulsion Laboratory, Caltech, under contract with the National Aeronautics and Space Administration.

The Sloan Digital Sky Survey (SDSS) is a joint project of The University of Chicago, Fermilab, the Institute for Advanced Study, the Japan Participation Group, The Johns Hopkins University, the Los Alamos National Laboratory, the Max-Planck-Institute for Astronomy (MPIA), the Max-Planck-Institute for Astrophysics (MPA), New Mexico State University, the United States Naval Observatory, the University of Pittsburgh, Princeton University, and the University of Washington. Apache Point Observatory, site of the SDSS telescopes, is operated by the Astrophysical Research Consortium (ARC).

Funding for the project has been provided by the Alfred P. Sloan Foundation, the SDSS member institutions, the National Aeronautics and Space Administration, the National Science Foundation, the U.S. Department of Energy, the Japanese Monbukagakusho, and the Max Planck Society. The SDSS Web site is <http://www.sdss.org/>.

REFERENCES

- Bahcall N. A., et al., 2003, preprint (astro-ph/0305202)
- Barger A. J., Aragon-Salamanca A., Ellis R. S., Couch W. J., Smail I., Sharples R. M., 1996, MNRAS, 279, 1
- Barkana R., Haiman Z., Ostriker J. P., 2001, ApJ, 558, 482
- Beers T. C., Flynn K., Gebhardt K., 1990, AJ, 100, 32
- Benson A. J., Frenk C. S., Baugh C. M., Cole S., Lacey C. G., 2002, preprint (astro-ph/0210354)
- Bernardi M. et al., 2003, AJ, 125, 1817
- Bernardi M. et al., 2003, AJ, 125, 1849
- Bernardi M. et al., 2003, AJ, 125, 1866
- Blanton M. R. et al., 2003, AJ, 125, 2348
- Blumenthal G. R., Faber S. M., Flores R., Primack J. R., 1986, ApJ, 301, 27
- Bode P., Bahcall N. A., Ford E. B., Ostriker J. P., 2001, ApJ, 551, 15
- Bond J. R., Cole S., Efstathiou G., Kaiser N., 1991, ApJ, 379, 440
- Borgani S., Governato F., Wadsley J., Menci N., Tozzi P., Quinn T., Stadel J., Lake G., 2002, MNRAS, 336, 409
- Bower R. G., 1991, MNRAS, 248, 332
- Bullock J. S., Kolatt, T. S., Sigad, Y., Somerville, R. S., Kravtsov, A. V., Klypin, A. A., Primack, J. R., Dekel, A., 2001, MNRAS, 321, 559
- Cole S., Kaiser N., 1989, MNRAS, 237, 1127
- Colless M., 1989, MNRAS, 237, 799
- Couch W. J., Sharples R. M., 1987, MNRAS, 229, 423
- Dalcanton J. J., Spergel D. N., Summers F. J., 1997, ApJ, 482, 659
- Danese L., de Zotti G., di Tullio G., 1980, A&A, 82, 322
- Davies R. L., Burstein D., Dressler A., Faber S. M.,

Lynden-Bell D., Terlevich R. J., Wegner G., 1987, *ApJS*, 64, 581

Davis M., Efstathiou G., Frenk C. S., White S. D. M., 1985, *ApJ*, 292, 371

Djorgovski S., Davis M., 1987, *ApJ*, 313, 59

Dressler A., 1980, *ApJ*, 236, 351

Dressler A., Lynden-Bell D., Burstein D., Davies R. L., Faber S. M., Terlevich R., Wegner G., 1987, *ApJ*, 313, 42

Ferrarese L., 2002, *ApJ*, 578, 90

Fukugita M., Ichikawa T., Gunn J. E., Doi M., Shimasaku K., Schneider D. P., 1996, *AJ*, 111, 1748

Fukugita M., Shimasaku K., Ichikawa T., 1995, *PASP*, 107, 945

Gerhard O., Kronawitter A., Saglia R. P., Bender R., 2001, *AJ*, 121, 1936

Ghigna S., Moore B., Governato F., Lake G., Quinn T., Stadel J., 1998, *MNRAS*, 300, 146

Ghigna S., Moore B., Governato F., Lake G., Quinn T., Stadel J., 2000, *ApJ*, 544, 616

Giovanelli R., Haynes M. P., Herter T., Vogt N. P., da Costa L. N., Freudling W., Salzer J. J., Wegner G., 1997, *AJ*, 113, 53

Girardi M., Mezzetti M., 2001, *ApJ*, 548, 79

Gnedin O. Y., Ostriker J. P., 2001, *ApJ*, 561, 61

Gomez P. et al., 2002, preprint (astro-ph/0210193)

Gonzalez A. H., Williams K. A., Bullock J. S., Kolatt T. S., Primack J. R., 2000, *ApJ*, 528, 145

Goto T. et al., 2002, *PASJ*, 54, 515

Governato F., Moore B., Cen R., Stadel J., Lake G., Quinn T., 1997, *New Astronomy*, 2, 91

Governato F., Baugh C. M., Frenk C. S., Cole S., Lacey C. G., Quinn T., Stadel J., 1998, *Nature*, 392, 359

Gunn J. E. et al., 1998, *AJ*, 116, 3040

Hayashi E., Navarro J. F., Taylor J. E., Stadel J., Quinn T., 2002, *ApJ*, preprint (astro-ph/0203004)

Hernquist L., 1990, *ApJ*, 356, 359

Hui L., 2001, *Physical Review Letters*, 86, 3467

Jenkins A., Frenk C. S., White S. D. M., Colberg J. M., Cole S., Evrard A. E., Couchman H. M. P., Yoshida N., 2001, *MNRAS*, 321, 372

Kaiser N., 1984, *ApJ*, 284, L9

Katz N., White S. D. M., 1993, *ApJ*, 412, 455

Klypin A., Gottlöber S., Kravtsov A. V., Khokhlov A. M., 1999, *ApJ*, 516, 530

Kochanek C. S., White M., 2001, *ApJ*, 559, 531

Kronawitter A., Saglia R. P., Gerhard O., Bender R., 2000, *A&AS*, 144, 53

Lacey C., Cole S., 1993, *MNRAS*, 262, 627

Lupton R. H., Gunn J. E., Ivezić Z., Knapp G. R., Kent S., Yasuda N., 2001, in *ASP Conf. Ser. 238: Astronomical Data Analysis Software and Systems X Vol. 10, The SDSS Imaging Pipelines*. pp 269–+

Mac Low M., Ferrara A., 1999, *ApJ*, 513, 142

Miller C. J. et al., 2001, *AJ*, 122, 3492

Miralda-Escudé J., 2002, *ApJ*, 564, 60

Mo H. J., Mao S., White S. D. M., 1998, *MNRAS*, 295, 319-336

Moore B., Katz N., Lake G., Dressler A., Oemler A., 1996, *Nature*, 379, 613

Moore B., Ghigna S., Governato F., Lake G., Quinn T., Stadel J., Tozzi P., 1999, *ApJ*, 524, L19

Navarro J. F., Frenk C. S., White S. D. M., 1997, *ApJ*, 490, 493

Nichol R. C. et al., 2001, in *Mining the Sky SDSS-RASS: Next Generation of Cluster-Finding Algorithms*.

Okamoto T., Habe A., 2000, *PASJ*, 52, 457

Poggianti B. M., Smail I., Dressler A., Couch W. J., Barger A. J., Butcher H., Ellis R. S., Oemler A. J., 1999, *ApJ*, 518, 576

Press W. H., Schechter P., 1974, *ApJ*, 187, 425

Quinn T., Katz N., Efstathiou G., 1996, *MNRAS*, 278, L49

Reed D., Gardner J., Quinn T., Stadel J., Fardal M., Lake G., Governato F., 2003, preprint (astro-ph/0301270)

Schlegel D. J., Finkbeiner D. P., Davis M., 1998, *ApJ*, 500, 525

Sheth R. K. et al., 2003, preprint (astro-ph/0304203)

Sheth R. K., Tormen G., 1999, *MNRAS*, 308, 119

Sheth R. K., Mo H. J., Tormen G., 2001, *MNRAS*, 323, 1

Shimasaku K., 1993, *ApJ*, 413, 59

Somerville R. S., 2002, *ApJ*, 572, L23

Somerville R. S., Primack J. R., 1999, *MNRAS*, 310, 1087

Springel V., White S. D. M., Tormen G., Kauffmann G., 2001, *MNRAS*, 328, 726

Stadel Y., 2001, PhD Thesis, Univ. Washington, Seattle

Stoughton C. et al., 2002, *AJ*, 123, 485

Strateva I. et al., 2001, *AJ*, 122, 1861

Tormen G., Diaferio A., Syer D., 1998, *MNRAS*, 299, 728

Tully R. B., Fouque P., 1985, *ApJS*, 58, 67

Tully R. B., Somerville R. S., Trentham N., Verheijen M. A. W., 2002, *ApJ*, 569, 573

White S. D. M., Tully R. B., Davis M., 1988, *ApJ*, 333, L45

White S. D. M., Davis M., Efstathiou G., Frenk C. S., 1987, *Nature*, 330, 451

York D. G. et al., 2000, *AJ*, 120, 1579

APPENDIX A: POPULATING SUBHALOS WITH GALAXIES

In order to estimate the effects of baryons on galaxy circular velocity profiles, we must know the circular velocity profiles of both the dark matter halo and the embedded collapsed baryons. A full description of the baryonic mass distribution requires knowledge not only of the density profile shape (galaxy type), but also a normalization (total galaxy mass) and a scalelength (galaxy size). In the remainder of this section, we outline our method for assigning galaxy types, masses, and sizes to the population of subhalos identified in the zero-redshift output of our highest resolution cluster simulation. Once the dark matter and baryon density profiles are fully specified, it is straightforward to compute the final rotation curve due to both components.

A0.1 Assigning Galaxy Types

Although galaxies exhibit a range of bulge-to-disk ratios, for simplicity we assign either a pure spheroidal or a pure disk baryonic component to each subhalo in the HR Virgo simulation. Spheroidals are described by a Hernquist density profile (Hernquist 1990):

$$\rho(r) = \frac{M_{\text{sph}} R_{\text{sph}}}{2\pi} \frac{1}{r (r + R_{\text{sph}})^3}, \quad (\text{A1})$$

where M_{sph} is the total mass of the spheroid, and the scale-length R_{sph} is related to the projected half-light radius R_0 of a deVaucouleurs surface brightness profile by $R_{\text{sph}} = 0.551R_0$.

Late type galaxies are assumed to be infinitely thin, and have surface density profiles of the form

$$\Sigma(r) = \frac{M_d}{2\pi R_d^2} e^{-r/R_d}, \quad (\text{A2})$$

where M_d is the total mass of the disk and R_d is the disk scale length.

$$M_d = 2\pi\Sigma_0 R_d^2. \quad (\text{A3})$$

Observationally, galaxy type is a function of circular velocity, with early type galaxies dominating at high V_c (Shimasaku 1993; Kochanek & White 2001; Sheth et al. 2003). Only the peak circular velocity of the dark matter component, V_{pk} , can be measured for each subhalo. We therefore assume that if early type galaxies dominate at high V_c , they also dominate at high V_{pk} . We randomly assign each subhalo the designation of early or late type based upon the early type fraction as a function of V_{pk} , $f_{\text{early}}(V_{\text{pk}})$. For simplicity we adopt a step function for $f_{\text{early}}(V_{\text{pk}})$.

$$f_{\text{early}}(V_{\text{pk}}) = \begin{cases} 0 & : V_{\text{pk}} < V_{\text{break}} \\ 1 & : V_{\text{pk}} \geq V_{\text{break}} \end{cases}, \quad (\text{A4})$$

where $125 \text{ km s}^{-1} < V_{\text{break}} < 150 \text{ km s}^{-1}$. Alternative functional forms which provide smoother transitions in the run of galaxy type with V_{pk} do not produce significantly different results. Substantially different values of V_{break} produce disagreement with the joint distribution of R_0 and σ_0 found by Bernardi et al. (2003) (see §A0.3).

A0.2 Assigning Galaxy Masses

In the previous subsection, we described our procedure for assigning either a Hernquist or exponential density profile to each subhalo. Each of these two profiles is parametrized by both a mass in collapsed baryons (M_{sph} or M_d) and a scale length (R_{sph} or R_d). We set the baryonic mass embedded within each subhalo equal to a fraction of the virial mass of that subhalo at the time that the baryons collapsed.

The first step towards determining the mass in cooled baryons embedded within each subhalo is to determine the virial mass of each subhalo. The virial radius of a simulated dark matter halo is usually taken to be the R_{200} , the radius interior to which the average density is equal to 200 times the critical density. The virial mass is then estimated as M_{200} , the mass interior to R_{200} . For subhalos, R_{200} , and therefore M_{200} is very difficult to measure. In addition, the baryons likely collapsed prior to the subhalo falling into the cluster and suffering the dynamical effects therein. We are therefore interested in the value of M_{200} for each subhalo before cluster incorporation. Although the cluster environment can lead to significant mass stripping, the peak circular velocities of halos (V_{pk}) remain relatively constant (Hayashi et al. 2002). We can therefore use the values of V_{pk} measured in the redshift zero simulation output to infer M_{200} using a correlation between the two found by Navarro, Frenk & White (1997):

$$\log\left(\frac{M_{200}}{10^{10} M_\odot}\right) = 3.23 \log\left(\frac{V_{\text{pk}}}{\text{km s}^{-1}}\right) - 5.31. \quad (\text{A5})$$

Once M_{200} has been determined for each subhalo, the second step is to specify the fraction, f_{cool} of M_{200} that winds up as cooled baryons. For late-type galaxies, we adopt the fitting function found by Gonzalez et al. (2000) in an analysis of the semi-analytic models of Somerville & Primack (1999):

$$f_{\text{cool}} \simeq 0.1 \left(\frac{x - 0.25}{1 + x^2}\right), \quad (\text{A6})$$

where $x = V_{\text{pk}}/(200 \text{ km s}^{-1})$. The above is valid for late type galaxies with $V_{\text{pk}} \simeq 60 - 350 \text{ km s}^{-1}$. For subhalos with $V_{\text{pk}} \leq 60 \text{ km s}^{-1}$, we set $f_{\text{cool}} = 0.02$. This minimum value of f_{cool} does not affect our comparison to observations, as subhalos with $V_{\text{pk}} \leq 60 \text{ km s}^{-1}$ are unlikely to have $V_c > V_{\text{comp1}}$. For early type galaxies, we explore $f_{\text{cool}} = 0.025, 0.05, 0.1$.

A0.3 Early Type Galaxy Sizes

In the previous two sections, we presented simple prescriptions for assigning a density profile shape and normalization to each subhalo within our highest resolution cluster simulation. Before the effects of baryons on galaxy rotation curves can be explored, we must assign scale lengths to the baryonic component of each subhalo. One projection of the Fundamental Plane tells us that the line of sight velocity dispersions, σ_{los} , or early type galaxies are correlated with their half-light radii, R_e , which are in turn simply related to the scale length of a Hernquist density profile. Under the assumption that σ_{los} is also correlated with the peak circular velocities V_{pk} of the dark matter halos in which they form, we can relate R_{sph} to V_{pk} .

In order to assign values of R_{sph} to each subhalo, we first assign values of R_0 . Using the full covariance matrix from B03, we draw one (σ_{los}, R_0) pair for each subhalo selected through the procedure described in §A0.1 to host an early type galaxy. Each value of R_0 is assigned a rank, with the largest R_0 receiving a rank of 1. Ranks are similarly assigned for each drawn σ_{los} and for each subhalo based upon its measured V_{pk} . Although we do not know the relationship between σ_{los} and V_{pk} , we expect both to correlate with R_0 . Thus, we assign each (σ_{los}, R_0) pair to a subhalo that has the same rank as that of the σ_{los} in that pair. This method of assigning sizes to subhalos preserves the scatter in the correlation between σ_{los} and R_0 , but assumes a perfect correlation between σ_{los} and V_{pk} .

Once values of R_0 have been assigned to each subhalo, R_{sph} is determined through $R_{\text{sph}} = 0.551R_0$.

A0.4 Late Type Galaxy Sizes

Our statistical assignment of early type galaxy sizes to subhalos was driven by observed correlations. For disk galaxies, if baryons initially share the spatial and angular momentum distribution of their host dark matter halo, and conserve angular momentum as they collapse, the resulting scalelength is related to the properties of the dark matter halo (Dalcanton et al. 1997; Mo, Mao & White 1998). We use this idea to assign a scale length, R_d , to each subhalo chosen to host a late type galaxies. Mo, Mao & White (1998) show that

$$R_d = \frac{1}{\sqrt{2}} \frac{j_d}{f_{\text{cool}}} \lambda r_{200} f_c^{-1/2} f_R, \quad (\text{A7})$$

where j_d is the fraction of the total halo angular momentum contained in the disk; f_{cool} is, as before, the fraction of the dark matter mass contained in cooling baryons; λ is the spin parameter of the dark matter halo; and r_{200} is the virial radius. Additionally,

$$f_c \simeq \frac{2}{3} + \left(\frac{c}{21.5}\right)^{0.7}, \quad (\text{A8})$$

where c is the halo concentration and

$$f_R \simeq \left(\frac{f_{\text{cool}}}{j_d} \frac{\lambda}{0.1}\right)^{(-0.06+2.71f_{\text{cool}}+0.0047f_{\text{cool}}/(j_d\lambda))} \quad (\text{A9})$$

$$\times (1 - 0.019c + 0.00025c^2 + 0.52/c) \quad (\text{A10})$$

We have specified f_{cool} in §A0.2, and we assume that $j_d = f_{\text{cool}}$. Bullock et al. (2001) analyze a $60 h^{-1}$ Mpc simulation carried out with the adaptive refinement tree N-body code, and found that the average halo spin parameter, $\bar{\lambda} = 0.04$, independent of V_{pk} . They also find the following relation for halo concentration:

$$c \approx 14 \sqrt{\frac{V_{\text{pk}}}{200 \text{ km s}^{-1}}} \quad (\text{A11})$$

Finally, r_{200} is the radius within which the average halo density is 200 times the critical density. It can be calculated straightforwardly from M_{200} , the mass enclosed within this radius:

$$r_{200} = \left(\frac{3M_{200}}{800\pi\rho_{\text{crit}}}\right)^{1/3}, \quad (\text{A12})$$

where $\rho_{\text{crit},0} \approx 136M_{\odot} \text{ kpc}^{-3}$ is the critical density of the universe and M_{200} is determined from Equation §A5.